X-ray analyzer-based phase-contrast computed laminography

Keiichi Hirano,* Yumiko Takahashi, Kazuyuki Hyodo and Masao Kimura

Institute of Materials Structure Science, High Energy Accelerator Research Organization, 1-1, Oho, Tsukuba, Ibaraki 305-0801, Japan. *Correspondence e-mail: keiichi.hirano@kek.jp

X-ray analyzer-based phase-contrast imaging is combined with computed laminography for imaging regions of interest in laterally extended flat specimens of weak absorption contrast. The optics discussed here consist of an asymmetrically cut collimator crystal and a symmetrically cut analyzer crystal arranged in a nondispersive $(+, -)$ diffraction geometry. A generalized algorithm is given for calculating multi-contrast (absorption, refraction and phase contrast) images of a sample. Basic formulae are also presented for laminographic reconstruction. The feasibility of the method discussed was verified at the vertical wiggler beamline BL-14B of the Photon Factory. At a wavelength of 0.0733 nm, phase-contrast sectional images of plastic beads were successfully obtained. Owing to strong circular artifacts caused by a sample holder, the field of view was limited to about 6 mm in diameter.

1. Introduction

When an X-ray beam passes through an object, its propagation direction is slightly refracted owing to the inhomogeneous electron density in the object. In X-ray analyzer-based imaging, this small refraction is detected by an analyzer crystal for nondestructive observation of inner structures of the object (Davis *et al.*, 1995; Chapman *et al.*, 1997). As the refraction contrast is mathematically equivalent to the differential phase contrast, X-ray analyzer-based imaging has much higher sensitivity to low-Z elements compared with conventional imaging techniques based on absorption contrast. On account of this advantage, X-ray analyzer-based phase-contrast imaging is widely used for observing various specimens, such as biological soft tissues and soft materials, at many synchrotron radiation facilities.

In X-ray imaging, volume reconstruction is usually carried out using computed tomography (CT) (Hounsfield, 1973). There are, however, several problems with the standard CT methods. The first problem is that the sample size must be smaller than the field of view (FOV) of the detector and beam size, which is generally a few centimeters when using synchrotron radiation (SR). This limitation has hindered the application of SR-CT to large samples. The second problem is that the thickness of the sample must be small enough for measuring the intensity of transmitted X-rays with sufficient accuracy. To mitigate these problems, synchrotron radiation computed laminography (SR-CL) was developed (Helfen *et al.*, 2005, 2011) by adopting the principles of tomosynthesis (Dobbins & Godfrey, 2003). Whereas the standard CT methods are characterized by tomographic rotation around an axis perpendicular to the beam path, SR-CL is characterized by the more general geometry of an inclined rotation axis. On account of this generalized geometry, SR-CL is applicable to a
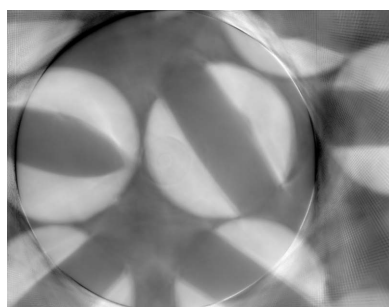
wider variety of samples compared with SR-CT. For example, SR-CL is especially effective for observing regions of interest (ROIs) in laterally extended samples such as flip-chip bonded devices (Helfen *et al.*, 2011), leaves (Verboven *et al.*, 2015) and thin organic objects (Krug *et al.*, 2008).

Since its development, SR-CL has been applied not only to microscopy (Watanabe *et al.*, 2009; Hoshino *et al.*, 2011; Xu *et al.*, 2012) but also to phase-contrast imaging based on propagation (Helfen *et al.*, 2009) and grating interferometry (Harasse *et al.*, 2010; Altapova *et al.*, 2012). Recently it was shown that analyzer-based phase-contrast imaging provides a better sensitivity with respect to propagation-based and grating-based phase-contrast imaging under certain experimental conditions (Diemoz *et al.*, 2012a,b). Furthermore, analyzer-based phase-contrast imaging is free from the phase unwrapping problem (Judge & Bryanston-Cross, 1994) associated with the fringe-scanning method (Bruning *et al.*, 1974) used in grating-based phase-contrast imaging. Because of these advantages, the combination of X-ray analyzer-based phase-contrast imaging and SR-CL is expected to be very useful.

Currently, two kinds of X-ray optics are mainly used for analyzer-based phase-contrast imaging: optics that make use of a pencil-beam and optics that make use of an expanded beam. Whereas a symmetrically cut collimator crystal is used in the former, an asymmetrically cut collimator crystal is used in the latter for expanding the beam. Because a large field of view is desirable for observing a large sample, we have used the latter optics so far (Hirano, 2003, 2011). Another advantage of the asymmetrically cut collimator crystal is that it has a larger acceptance angle than the symmetrically cut collimator crystal. We have also developed a generalized algorithm for obtaining multi-contrast (absorption, refraction and phase contrast) images.

In this paper, we propose the introduction of SR-CL to analyzer-based phase-contrast imaging for observing ROIs in laterally extended flat samples of weak absorption contrast. We also describe our generalized algorithm for obtaining multi-contrast images of a sample, and present the basic formulae for laminographic reconstruction.

2. Theoretical background

2.1. Optical setup

An optical setup of X-ray analyzer-based phase-contrast computed laminography is schematically shown in Fig. 1. The optics consist of an asymmetrically cut first crystal (collimator) and a symmetrically cut second crystal (analyzer) arranged in a nondispersive (+, −) diffraction geometry. In this optics, the diffraction plane is defined as the plane that includes the optical path. The incident monochromatic X-ray beam is collimated and expanded in the diffraction plane by the first crystal and propagates

through the sample. The refraction caused by the sample is analyzed by the second crystal. The beam diffracted by the second crystal is observed by an X-ray area detector.

Here, we introduce the laboratory coordinate systems (x_1, y_1, z_1) for the sample and (x_2, y_2, z_2) for the detector as shown in Fig. 1. Here the z_j axis ($j = 1, 2$) is antiparallel to the beam direction and the y_j axis ($j = 1, 2$) is perpendicular to the diffraction plane. Using these coordinate systems, we can define an object plane ($x_1 y_1$ plane) right after the sample and a detector plane ($x_2 y_2$ plane) right before the detector. Notice that a point (p, q) in the object plane is projected by the analyzer to a point ($-p, q$) in the detector plane.

2.2. Principles of X-ray analyzer-based phase-contrast imaging

The optical properties of the sample are described by the complex refraction index $n = 1 - \delta + i\beta$. The phase shift produced by the sample is given by

$$\Phi(x_1, y_1) = \frac{2\pi}{\lambda} \int \delta(x_1, y_1, z_1)\, dz_1, \qquad (1)$$

where λ is the wavelength. The beam refraction due to the phase shift is given by $(\lambda/2\pi)\nabla_\perp \Phi$. The analyzer is only sensitive to the refraction component in the diffraction plane, which is given by

$$\psi_{x_1}(x_1, y_1) = \frac{\lambda}{2\pi} \frac{\partial \Phi}{\partial x_1} = \frac{\partial}{\partial x_1} \int \delta(x_1, y_1, z_1)\, dz_1. \qquad (2)$$

Because this equation is similar to a Radon transformation, we can estimate the δ function from a set of refraction maps using the volume reconstruction algorithm.

Before estimating the refraction map of the sample, $\psi_{x_1}(x_1, y_1)$, it is necessary to first measure the rocking curve of the analyzer without the sample. Fig. 2 shows an example of the rocking curve, $R_{\text{ref}}(\theta)$, measured at a reference point near the optical axis on the detector plane. (The profile of this rocking curve was obtained by the experiments described in §3.) Here, R_{ref} is the intensity of the diffracted beam and θ is the offset angle from the diffraction condition. According to
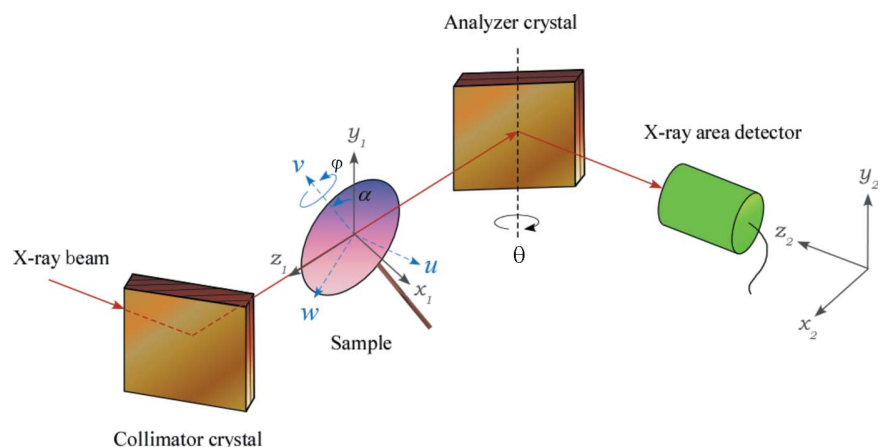
Figure 1
X-ray optics for analyzer-based phase-contrast computed laminography

the dynamical theory of X-ray diffraction (Zachariasen, 1945; Batterman & Cole, 1964; Ishikawa & Kohra, 1991; Authier, 2001), the full width at half-maximum (FWHM) of $R_{ref}(\theta)$ is usually in the order of 0.1–10 arcsec. In the case of X-ray optics that make use of a symmetrically cut collimator crystal, the shape of $R_{ref}(\theta)$ is close to triangular. However, in the case of our optics, which make use of an asymmetrically cut collimator crystal, $R_{ref}(\theta)$ is no longer triangular but close to the silk-hat shape of the intrinsic rocking curve. This is why it is necessary to use the generalized algorithm shown below for image analyses.

In general, the profile of the rocking curve gradually varies with the location of the measuring point. Here, we assume that the rocking curve measured at (x_2, y_2) without the sample is expressed as

$$R_{o}(\theta, x_2, y_2) = a_{o}(x_2, y_2)R_{ref}[\theta - b_{o}(x_2, y_2)], \qquad (3)$$

where $a_{o}(x_2, y_2)$ is proportional to the incident beam intensity and $b_{o}(x_2, y_2)$ is the shift amount. At the reference point, $a_{o} = 1$ and $b_{o} = 0$. Both $a_{o}(x_2, y_2)$ and $b_{o}(x_2, y_2)$ depend on the optical setting and experimental conditions. For the estimation of $a_{o}(x_2, y_2)$ and $b_{o}(x_2, y_2)$, it is necessary to acquire two images on each side of the rocking curve, one at the low-angle side, θ_{LO}, and one at the high-angle side, θ_{HO} (Fig. 2). The acquired images are represented by $R_{o}(\theta_{LO}, x_2, y_2)$ and $R_{o}(\theta_{HO}, x_2, y_2)$, respectively. Dividing the former by the latter, we can extract the effect of $b_{o}(x_2, y_2)$:

$$\frac{R_{o}(\theta_{HO}, x_2, y_2)}{R_{o}(\theta_{LO}, x_2, y_2)} = \frac{a_{o}(x_2, y_2)R_{ref}[\theta_{HO} - b_{o}(x_2, y_2)]}{a_{o}(x_2, y_2)R_{ref}[\theta_{LO} - b_{o}(x_2, y_2)]}$$
$$= \frac{R_{ref}[\theta_{HO} - b_{o}(x_2, y_2)]}{R_{ref}[\theta_{LO} - b_{o}(x_2, y_2)]}. \qquad (4)$$

For the estimation of $b_{o}(x_2, y_2)$, we introduce the following function:

$$V_{o}(\varepsilon) \equiv \frac{R_{ref}(\varepsilon + \Delta\theta_{o}/2)}{R_{ref}(\varepsilon - \Delta\theta_{o}/2)}, \qquad (5)$$

where $\Delta\theta_{o}$ is the difference between θ_{LO} and θ_{HO} ($\Delta\theta_{o} \equiv \theta_{HO} - \theta_{LO}$). $\Delta\theta_{o}$ is usually set around the FWHM of the rocking curve, $R_{ref}(\theta)$. For example, Fig. 3 shows the calculated $V_{o}(\varepsilon)$ curve from the rocking curve, $R_{ref}(\theta)$, shown in Fig. 2. Using this $V_{o}(\varepsilon)$ curve as a lookup table, we can estimate the ε value, ε_{o}, which corresponds to the measured value of $R_{o}(\theta_{HO}, x_2, y_2)/R_{o}(\theta_{LO}, x_2, y_2)$. Then we can obtain $b_{o}(x_2, y_2)$ by

$$b_{o}(x_2, y_2) = -\varepsilon_{o}(x_2, y_2) + \frac{\theta_{LO} + \theta_{HO}}{2}. \qquad (6)$$

As shown in Fig. 3, the estimation of ε_{o} is only possible in the limited region between ε_{L} and ε_{H}. The width of this region is approximately the FWHM of the rocking curve, $R_{ref}(\theta)$, and is usually sufficient for observing most samples. Once the $b_{o}(x_2, y_2)$ is obtained, $a_{o}(x_2, y_2)$ is given by

$$a_{o}(x_2, y_2) = \frac{R_{o}(\theta_{HO}, x_2, y_2)}{R_{ref}[\theta_{HO} - b_{o}(x_2, y_2)]}$$
$$= \frac{R_{o}(\theta_{LO}, x_2, y_2)}{R_{ref}[\theta_{LO} - b_{o}(x_2, y_2)]}. \qquad (7)$$

When the sample is inserted into the optical path, the X-ray beam is absorbed and refracted by the sample. Here, we disregard the effect of X-ray small-angle scattering. In this case, the rocking curve of the analyzer is expressed as

$$R_{s}(\theta, x_2, y_2) = a_{o}(x_2, y_2)\, t_{s}(x_2, y_2)\, R_{ref}[\theta - b_{o}(x_2, y_2) - r_{s}(x_2, y_2)], \qquad (8)$$

where $t_{s}(x_2, y_2)$ is the transmissivity and $r_{s}(x_2, y_2)$ is the refraction angle. The former corresponds to the absorption-contrast image (absorption map) and the latter to the refraction-contrast image (refraction map). We can estimate the refraction map, $r_{s}(x_2, y_2)$, from two images recorded at θ_{LS} and

Figure 2
An example of the rocking curve, $R_{ref}(\theta)$, measured at the reference point without the sample.
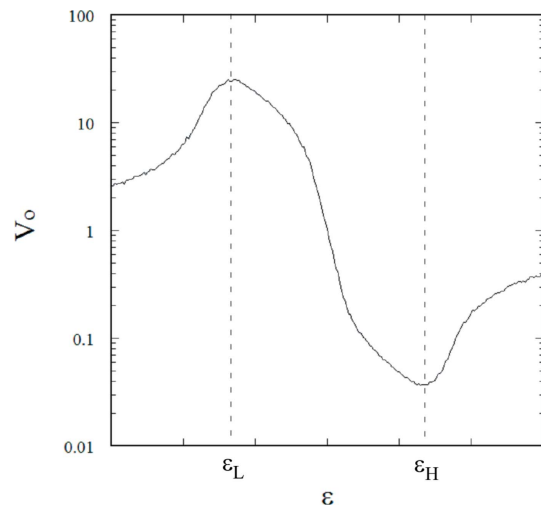
Figure 3
Example of the calculated $V_{o}(\varepsilon)$ curve from the rocking curve, $R_{ref}(\theta)$, shown in Fig. 2.

θ_{HS}. Dividing $R_s(\theta_{HS}, x_2, y_2)$ by $R_s(\theta_{LS}, x_2, y_2)$, we can extract the effect of $r_s(x_2, y_2)$,

$$\frac{R_s(\theta_{HS}, x_2, y_2)}{R_s(\theta_{LS}, x_2, y_2)} = \frac{R_{ref}[\theta_{HS} - b_o(x_2, y_2) - r_s(x_2, y_2)]}{R_{ref}[\theta_{LS} - b_o(x_2, y_2) - r_s(x_2, y_2)]}. \quad (9)$$

For the estimation of $r_s(x_2, y_2)$, we reintroduce the following function:

$$V_s(\varepsilon) \equiv \frac{R_{ref}(\varepsilon + \Delta\theta_s/2)}{R_{ref}(\varepsilon - \Delta\theta_s/2)}, \quad (10)$$

where $\Delta\theta_s$ is the difference between θ_{LS} and θ_{HS} ($\Delta\theta_s \equiv \theta_{HS} - \theta_{LS}$). Using this function as the lookup table, we can estimate the ε value, ε_s, which corresponds to the measured value of $R_s(\theta_{HS}, x_2, y_2)/R_s(\theta_{LS}, x_2, y_2)$. Then we can obtain $r_s(x_2, y_2)$ from

$$r_s(x_2, y_2) = \varepsilon_o(x_2, y_2) - \varepsilon_s(x_2, y_2) \\ + (\theta_{LS} + \theta_{HS} - \theta_{LO} - \theta_{HO})/2. \quad (11)$$

If $\theta_{LS} = \theta_{LO}$ and $\theta_{HS} = \theta_{HO}$, this equation is simplified as $r_s(x_2, y_2) = \varepsilon_o(x_2, y_2) - \varepsilon_s(x_2, y_2)$. Once $r_s(x_2, y_2)$ is obtained, $t_s(x_2, y_2)$ is given by

$$a_o(x_2, y_2)t_s(x_2, y_2) = \frac{R_s(\theta_{HS}, x_2, y_2)}{R_{ref}[\theta_{HS} - b_o(x_2, y_2) - r_s(x_2, y_2)]} \\ = \frac{R_s(\theta_{LS}, x_2, y_2)}{R_{ref}[\theta_{LS} - b_o(x_2, y_2) - r_s(x_2, y_2)]}. \quad (12)$$

Note that both $t_s(x_2, y_2)$ and $r_s(x_2, y_2)$ are the images on the detector plane. To obtain the corresponding images on the object plane (x_1y_1 plane), it is necessary to invert the images along the x_2 axis. Without this procedure, laminographic reconstruction will result in failure.

2.3. Laminographic reconstruction

For laminographic reconstruction, it is necessary to obtain a set of refraction maps by rotating the sample through $360°$. Here we introduce a coordinate system (u, v, w) attached to the sample as shown in Fig. 1. The rotation axis ($\hat{\varphi}$ axis) coincides with the v axis, and is tilted at angle α from the y_1 axis. When $\varphi = 0°$ and $\alpha = 0°$, the object coordinate system (u, v, w) coincides with the laboratory coordinate system (x_1, y_1, z_1). The relationship between the coordinates of a given point in the object coordinate system (u, v, w) and in the laboratory coordinate system (x_1, y_1, z_1) is given by

$$\begin{pmatrix} x_1 \\ y_1 \\ z_1 \end{pmatrix} = \begin{pmatrix} \cos\varphi & 0 & -\sin\varphi \\ \sin\alpha\sin\varphi & \cos\alpha & \sin\alpha\cos\varphi \\ \cos\alpha\sin\varphi & -\sin\alpha & \cos\alpha\cos\varphi \end{pmatrix} \begin{pmatrix} u \\ v \\ w \end{pmatrix}. \quad (13)$$

X-ray laminographic reconstruction is based on the filtered backprojection method and is represented by the following equation,

$$\delta_{fbp}(u, v, w) = \frac{1}{2\pi} \int_0^{2\pi} p(\varphi, x_1, y_1) \, d\varphi,$$

$$\begin{cases} x_1 = u\cos\varphi - w\sin\varphi, \\ y_1 = u\sin\alpha\sin\varphi + v\cos\alpha + w\sin\alpha\cos\varphi, \end{cases} \quad (14)$$

where $p(\varphi, x_1, y_1)$ is a filtered projection image for each φ angle. A reconstructed sectional image of δ_{fbp} at a given v value is parallel to the uw plane. The three-dimensional volume data can be obtained by stacking the reconstructed images along the v axis. The filtered projection image, $p(\varphi, x_1, y_1)$, is given by

$$p(\varphi, x_1, y_1) = \int \left[\int \psi_{x_1}(\varphi, x_1, y_1) \exp(-2\pi i x_1 \omega) \, dx_1 \right] \\ \times H(\omega) \exp(2\pi i x_1 \omega) \, d\omega, \quad (15)$$

where $\psi_{x_1}(\varphi, x_1, y_1)$ is the refraction map on the object plane and $H(\omega)$ is the one-dimensional filter function. This equation can be simply expressed as

$$p(\varphi, x_1, y_1) = F^{-1}[F(\psi_{x_1}) \times H], \quad (16)$$

where F denotes the one-dimensional Fourier transform and F^{-1} the one-dimensional inverse Fourier transform. The filter function is given by

$$H(\omega) = -i\frac{\cos\alpha}{2}\text{sgn}(\omega) \quad (17)$$

with

$$\text{sgn}(\omega) = \begin{cases} -1 & \text{if} \quad \omega < 0 \\ 0 & \text{if} \quad \omega = 0 \\ +1 & \text{if} \quad \omega > 0 \end{cases}$$

(Harasse *et al.*, 2010).

Note that this laminographic reconstruction is the generalization of the tomosynthetic approach (Maksimenko *et al.*, 2007). It is also worth noting that the δ_{fbp} given by equation (14) is only an approximation of δ due to (i) incomplete sampling in Fourier space and (ii) the filtering process in equation (15).

3. Experiments and results

To verify the feasibility of X-ray analyzer-based phase-contrast computed laminography, we performed experiments at the vertical wiggler beamline BL-14B of the Photon Factory. At first, the white beam from the light source was monochromated at 0.0733 nm by a Si(111) double-crystal monochromator. Then, the monochromatic beam linearly polarized in the vertical direction was incident to the X-ray optics shown in Fig. 1. For minimizing the intensity loss caused by the polarization effect, the diffraction plane of the optics was set in the horizontal plane. This means that the polarization of the incident beam corresponded to σ-polarization for the optics. For the collimator, we used an asymmetric Si(220) crystal. The angle between the crystal surface and the diffracting lattice planes was $10°$ and the Bragg angle was $11°$. As a result, the incident beam was expanded 10.9 times in the horizontal plane. Then the central part of the expanded beam was selected by a slit. For the analyzer, we used a symmetric Si(220) crystal. Both the collimator and the analyzer were made of non-doped float-zone silicon crystal ($\rho \geq 2000$ Ω cm), and their surfaces were mechanochemically polished in order to remove defects and strain fields. The beam diffracted by the

analyzer was recorded on a fiber-coupled X-ray CCD camera (Photonic Science Limited, X-ray FDI 1:1) consisting of a GdO_2S:Tb scintillator (7 mg cm^{-2}), a 1:1 glass fiber plate and a CCD. At the scintillator, X-rays were converted to visible light, which was transmitted through the glass fiber plate and detected by the CCD. The pixel size was 6.45 μm (H) × 6.45 μm (V) and the number of pixels was 1392 (H) × 1040 (V). The distance between the sample and the analyzer was about 25 cm, and the distance between the analyzer and the X-ray CCD camera was about 25 cm.

First, we measured the rocking curve of the analyzer without the sample. The aperture of the slit was set at 1 mm (H) × 1 mm (V) in size. The shape of the obtained rocking curve was close to the silk-hat shape of the intrinsic rocking curve. The FWHM was estimated to be 2.5 arcsec. This value agrees well with the theoretical value of 2.3 arcsec. The slight discrepancy is considered to be caused by deformation of the collimator and/or analyzer. Next, we set the aperture of the slit at 10 mm (H) × 10 mm (V) in size, and recorded the beam diffracted by the analyzer at $\theta_{LO} = -1.25$ arcsec and $\theta_{HO} = +1.25$ arcsec. The exposure time was 1 s per image. Using the calculated $V_o(\varepsilon)$ curve as the lookup table, we estimated $b_o(x_2, y_2)$.

Then, we inserted a sample into the optical path. We used plastic beads made from acrylic resin as the sample. The diameter of each bead was about 3 mm. Fig. 4 is a photograph showing the area around the sample holder. The $\hat{\alpha}$ axis is on the horizontal plane and is perpendicular to the optical path. The φ stage was mounted on the α stage so that the $\hat{\varphi}$ axis would always become perpendicular to the $\hat{\alpha}$ axis and

perpendicular to the optical path at $\alpha = 0°$. In the experiments, we fixed the α angle at 30°. A photograph of the sample holder is also shown in the inset of Fig. 4. The sample holder was made by attaching an acrylic sheet to a polypropylene tube of 6 mm diameter with an adhesive made of dichloromethylene.

To obtain the refraction maps of the sample, we set the analyzer angle at $\theta_{LS} = \theta_{LO} = -1.25$ arcsec and $\theta_{HS} = \theta_{HO} = +1.25$ arcsec. It took less than a few seconds to change the analyzer angle and stabilize the analyzer crystal. At each analyzer angle we recorded a set of images by rotating the sample around the $\hat{\varphi}$ axis through 360° in 1° steps. The exposure time was 1 s per image and the total measurement time was ~30 min. About 60% of the measurement time was spent on rotation of the sample and data transfer from the X-ray CCD camera to the workstation. We will be able to reduce this dead time by using an X-ray detector with short readout time such as a scientific CMOS camera and by implementing an on-the-fly scan.

From the set of obtained refraction maps, we calculated the phase-contrast sectional images of the sample. Fig. 5 shows the results obtained at different depth positions: (a) $v = 0$ mm and (b) $v = 0.97$ mm. Depth-dependent features can be clearly seen, which shows that the laminographic reconstruction was successful. In each image, a strong circular artifact is also observed. These artifacts originate from the joint of the sample holder. Due to these artifacts, the FOV was limited to about 6 mm in diameter. Clear phase-contrast sectional images can be obtained as long as the ROI is located inside this FOV. We will be able to expand the FOV by replacing the
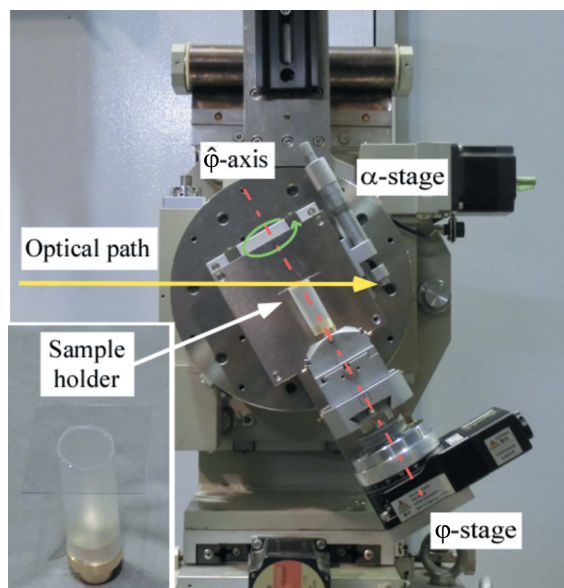
Figure 4
Photograph showing the area around the sample holder. The $\hat{\alpha}$ axis is in the horizontal plane and perpendicular to the optical path. The φ stage is mounted on the α stage so that the $\hat{\varphi}$ axis would always become perpendicular to the $\hat{\alpha}$ axis and perpendicular to the optical path at $\alpha = 0°$. The lower-left inset is a photograph of the sample holder. The sample holder is made by attaching an acrylic sheet to a polypropylene tube of 6 mm in diameter with an adhesive made of dichloromethylene.
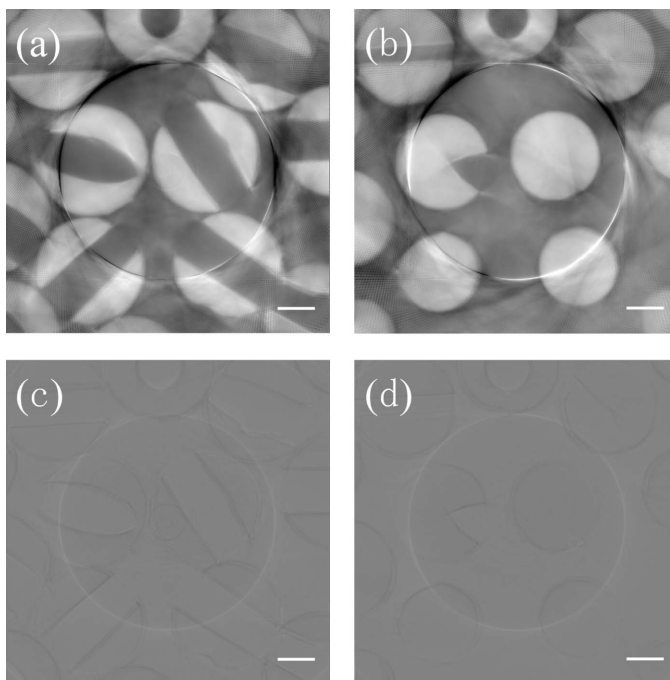
Figure 5
Reconstructed phase-contrast sectional images of the plastic beads at different depth positions: (a) $v = 0$ mm and (b) $v = 0.97$ mm. For comparison, corresponding absorption-contrast images are also shown in (c) and (d). The strong circular artifact in each image originates from the joint of the sample holder. The size of each scale bar is 1 mm.

polypropylene tube of the sample holder with a larger one. For comparison, corresponding absorption-contrast images are also shown in Figs. 5(c) and 5(d). The phase-contrast images are much clearer than the absorption-contrast images. It is also seen that the edge of each bead is slightly enhanced due to Fresnel diffraction in Figs. 5(c) and 5(d).

In this study, we assumed that the effect of ultra-small-angle X-ray scattering (USAX) caused by a sample is negligible. Regarding the plastic beads used in our experiment, this assumption is valid. However, for a sample where this assumption is no longer valid, our approach will not provide a correct image. For such a sample, multiple-image radiography (Pagot et al., 2003) will be useful for obtaining correct multi-contrast (absorption, refraction, USAX and phase contrast) sectional images.

4. Conclusion

We have developed X-ray analyzer-based phase-contrast computed laminography for imaging ROIs in laterally expanded flat specimens of weak absorption contrast. Our optics consist of an asymmetrically cut collimator crystal and a symmetrically cut analyzer crystal arranged in a nondispersive $(+, -)$ diffraction geometry. We showed the generalized algorithm for calculating multi-contrast (absorption, refraction and phase contrast) images of a sample. Furthermore, we presented the basic formulae for laminographic reconstruction. In the experiments performed at the vertical wiggler beamline BL-14B of the Photon Factory, we successfully obtained phase-contrast sectional images of the plastic bead sample at a wavelength of 0.0733 nm. Strong circular artifacts originating from the joint of the sample holder were also observed. Due to these artifacts, the FOV was limited to about 6 mm in diameter. It will be possible to enlarge the FOV by replacing the polypropylene tube of the sample holder with a larger one.

References

Altapova, V., Helfen, L., Myagotin, A., Hänschke, D., Moosmann, J., Gunneweg, J. & Baumbach, T. (2012). Opt. Express, 20, 6496–6508.

Authier, A. (2001). Dynamical Theory of X-ray Diffraction. New York: Oxford University Press.

Batterman, B. W. & Cole, H. (1964). Rev. Mod. Phys. 36, 681–717.

Bruning, J. H., Herriott, D. R., Gallagher, J. E., Rosenfeld, D. P., White, A. D. & Brangaccio, D. J. (1974). Appl. Opt. 13, 2693–2703.

Chapman, D., Thomlinson, W., Johnston, R. E., Washburn, D., Pisano, E., Gmür, N., Zhong, Z., Menk, R., Arfelli, F. & Sayers, D. (1997). Phys. Med. Biol. 42, 2015–2025.

Davis, T. J., Gao, D., Gureyev, T. E., Stevenson, A. W. & Wilkins, S. W. (1995). Nature (London), 373, 595–598.

Diemoz, P. C., Bravin, A. & Coan, P. (2012a). Opt. Express, 20, 2789–2805.

Diemoz, P. C., Bravin, A., Langer, M. & Coan, P. (2012b). Opt. Express, 20, 27670–27690.

Dobbins, J. T. III & Godfrey, D. J. (2003). Phys. Med. Biol. 48, R65–R106.

Harasse, S., Hirayama, N., Yashiro, W. & Momose, A. (2010). Proc. SPIE, 7804, 780411.

Helfen, L., Baumbach, T., Cloetens, P. & Baruchel, J. (2009). Appl. Phys. Lett. 94, 104103.

Helfen, L., Baumbach, T., Mikulík, P., Kiel, D., Pernot, P., Cloetens, P. & Baruchel, J. (2005). Appl. Phys. Lett. 86, 071915.

Helfen, L., Myagotin, A., Mikulík, P., Pernot, P., Voropaev, A., Elyyan, M., Di Michiel, M., Baruchel, J. & Baumbach, T. (2011). Rev. Sci. Instrum. 82, 063702.

Hirano, K. (2003). J. Phys. D, 36, 1469–1472.

Hirano, K. (2011). Jpn. J. Appl. Phys. 50, 026402.

Hoshino, M., Uesugi, K., Takeuchi, A., Suzuki, Y. & Yagi, N. (2011). Rev. Sci. Instrum. 82, 073706.

Hounsfield, G. N. (1973). Br. J. Radiol. 46, 1016–1022.

Ishikawa, T. & Kohra, K. (1991). Handbook on Synchrotron Radiation, Vol. 3, edited by G. S. Brown and D. E. Moncton, pp. 63–104. Amsterdam: North-Holland.

Judge, T. R. & Bryanston-Cross, P. J. (1994). Opt. Lasers Eng. 21, 199–239.

Krug, K., Porra, L., Coan, P., Wallert, A., Dik, J., Coerdt, A., Bravin, A., Elyyan, M., Reischig, P., Helfen, L. & Baumbach, T. (2008). J. Synchrotron Rad. 15, 55–61.

Maksimenko, A., Yuasa, T., Ando, M. & Hashimoto, E. (2007). Appl. Phys. Lett. 91, 234108.

Pagot, E., Cloetens, P., Fiedler, S., Bravin, A., Coan, P., Baruchel, J., Härtwig, J. & Thomlinson, W. (2003). Appl. Phys. Lett. 82, 3421–3423.

Verboven, P., Herremans, E., Helfen, L., Ho, Q. T., Abera, M., Baumbach, T., Wevers, M. & Nicolaï, B. M. (2015). Plant J. 81, 169–182.

Watanabe, N., Hoshino, M., Yamamoto, K., Aoki, S., Takeuchi, A. & Suzuki, Y. (2009). AIP Conf. Ser. 186, 012022.

Xu, F., Helfen, L., Suhonen, H., Elgrabli, D., Bayat, S., Reischig, P., Baumbach, T. & Cloetens, P. (2012). PLoS One, 7, e50124.

Zachariasen, W. H. (1945). Theory of X-ray Diffraction in Crystals. New York: Wiley.